International Journal of Solids and Structures 54 (2015) 31–41

Contents lists available at ScienceDirect

International Journal of Solids and Structures

journal homepage: www.elsevier.com/locate/ijsolstr

Interfacial imperfection coupling model with application to the in-plane fracture problem of a multiferroic composite

Yong-Dong Li [a,*], Tao Xiong [a], Li-Hong Dong [b]

[a] Department of Mechanical Engineering, Academy of Armored Force Engineering, Beijing 100072, PR China
[b] National Key Laboratory for Remanufacturing, Academy of Armored Force Engineering, Beijing 100072, PR China

ARTICLE INFO

Article history:
Received 23 June 2014
Received in revised form 14 October 2014
Available online 20 November 2014

Keywords:
Multiferroic composites
Interfacial imperfection coupling model
Spring model
Fracture
Piezomagnetic/piezoelecrtric materials

ABSTRACT

A coupling model is proposed to characterize interfacial imperfections by generalizing the spring model and referring to the magneto-electro-elastic constitutive relations. As an application, in-plane fracture analysis is performed on a multiferroic composite, which consists of a ferromagnetic layer, a ferroelectric layer and an imperfect interfacial region. The methods of Fourier integral transform and Green's function are employed to derive the Cauchy singular integral equations for the cracks. Numerical results of the mechanical strain energy release rate are provided to survey the effects of interfacial imperfections and their couplings. It is found that imperfection couplings affect the fracture behavior remarkably and so it is necessary to consider them in the mechanical problems of this kind of smart structures.

1. Introduction

For most composites in engineering, the interfaces are key parts that play important role in not only bonding different constituents together but also transferring loads. However, they are meanwhile relatively weak regions that is prone to losing their functions due to the nucleation, growth and coalescence of the interfacial voids, flaws and imperfections (Needleman, 1987, 1990). Therefore, the researches on imperfect interfaces have formed an active branch of composite studies in the past decades (Hashin, 1990; Benveniste and Miloh, 2001; Nairn, 2007; Vellender et al., 2013; Kushch and Chernobai, 2014). In classical theories of mechanics, an imperfect interface is generally modeled as a spring-type medium, across which the normal and tangential stresses are continuous but the displacements are discontinuous. The jumps of displacements are employed to characterize the interfacial imperfections and the stress components are assumed to be proportional to the jumps of the corresponding displacement components (Hashin, 1991; Chen et al., 2004; Guessasma et al., 2010; Rizzoni and Lebon, 2013; Li and Jin, 2014). For example, the spring-type model of an imperfect interface Γ, lying along the x-axis and normal to the z-axis, can be formulated as (Sudak et al., 1999; Hashin, 2002; Fan and Wang, 2003; Wang et al., 2008; Zhong et al., 2009a)

$$\left.\begin{aligned}\sigma_{zz}|_{\Gamma^+} + \mathrm{i}\tau_{zx}|_{\Gamma^+} &= \sigma_{zz}|_{\Gamma^-} + \mathrm{i}\tau_{zx}|_{\Gamma^-}\\ \sigma_{zz}|_{\Gamma} + \mathrm{i}\tau_{zx}|_{\Gamma} &= k_\sigma(w|_{\Gamma^+} - w|_{\Gamma^-}) + \mathrm{i}k_\tau(u|_{\Gamma^+} - u|_{\Gamma^-})\end{aligned}\right\} \tag{1}$$

where i is the imaginary unit. σ and τ are the normal and tangential stress components. w and u are the displacement components along the z-axis and x-axis. k_σ and k_τ are the nonnegative stiffness coefficients of the interface, which are zero in the case of a completely debonded interface and tend to infinity when the interface is perfectly bonded.

With the wider and wider applications of layered smart structures and devices in engineering, the problems of imperfect interfaces in piezomagnetic/piezoelectric composites have also drawn much attention of researchers in the past years, (Chen and Lee, 2004; Huang et al., 2009; Fang et al., 2009; Gu and He, 2011; Yuan et al., 2014). Under harsh in situ conditions, the interfaces in these smart composites might be damaged mechanically, magnetically and electrically (Benveniste, 2009; Li and Lee, 2009; Sun et al., 2011), i.e., they might become not only mechanically debonded but also magnetically and electrically impermeable. The spring-type model is generalized to formulate the mechanical, electric and magnetic interfacial imperfections by simply assuming that the generalized stress is continuous while the generalized displacement is discontinuous across the interface and the former is proportional to the jump of the latter. Again, suppose that the imperfect interface Γ lies along the x-axis and normal to the z-axis. Then, the generalized spring-type model takes the form (Wang and

* Corresponding author. Tel.: +86 10 6671 7248.
E-mail address: LYDbeijing@163.com (Y.-D. Li).

http://dx.doi.org/10.1016/j.ijsolstr.2014.11.010
0020-7683/

Pan 2007; Sun et al., 2011; Wang, 2011; Otero et al., 2012, 2013; Gu et al., 2014; Liu et al., 2014; Wang et al., 2014)

$$\left.\begin{aligned}\boldsymbol{\sigma}_z|_{\Gamma^+} &= \boldsymbol{\sigma}_z|_{\Gamma^-}\\ \boldsymbol{\sigma}_z|_{\Gamma} &= \mathbf{K}_\Gamma(\mathbf{u}|_{\Gamma^+} - \mathbf{u}|_{\Gamma^-})\end{aligned}\right\} \tag{2}$$

where $\boldsymbol{\sigma}_z$ is the generalized stress and $\mathbf{u}$ the generalized displacement. $\boldsymbol{\sigma}_z = [\tau_{zx} \quad \sigma_{zz} \quad B_z \quad D_z]^{\mathrm{T}}$ with τ_{zx}, σ_{zz}, B_z and D_z being the shear stress, normal stress, normal magnetic induction and normal electric displacement, respectively. $\mathbf{u} = [u \quad w \quad \varphi \quad \phi]^{\mathrm{T}}$ with φ and ϕ representing the magnetic potential and electric potential. $\mathbf{K}_\Gamma$ is the generalized stiffness matrix composed of the four interfacial parameters k_τ, k_σ, k_B and k_D as follows

$$\mathbf{K}_\Gamma = \begin{bmatrix} k_\tau & 0 & 0 & 0\\ 0 & k_\sigma & 0 & 0\\ 0 & 0 & -k_B & 0\\ 0 & 0 & 0 & -k_D \end{bmatrix} \tag{3}$$

Like in the classical case, the interfacial parameters vanish when the interface is not only mechanically debonded but also magnetically and electrically impermeable; they become infinity if the interface is perfectly bonded and meanwhile magnetically and electrically permeable. The imperfect interface complying with the generalized spring-type model in Eq. (2) is also called a mechanically soft and dielectrically/magnetically weakly conducting interface (Kuo, 2013).

Although the generalized linear spring model (GLSM) in Eqs. (2) and (3) reflects the main feature of the imperfect interface in piezomagnetic/piezoelectric composites, it ignores the interactions among the mechanical, magnetic and electric imperfections. Eqs. (2) and (3) indicate that these three kinds of interfacial imperfections occur and take effect independently. This is obviously inconsistent with the magneto-electro-mechanical coupling behavior of this kind of smart composites. As is known, magneto-electro-mechanical couplings exist via the interfaces in the composites consisting of alternate piezoelectric and piezomagnetic layers (Zheng et al., 2004; Spaldin and Fiebig, 2005; Eerenstein et al., 2006; Bichurin et al., 2007). So, it is natural to infer that similar couplings may also exist among the mechanical, magnetic and electric imperfections in the interfacial region, that is to say, any one of them cannot independently exist and will necessarily give rise to the other two ones. However, these couplings have been scarcely studied and only the coupling between mechanical and electric imperfections in the interfaces of a particulate piezoelectric composite has been dealt with in the latest work of Shi et al. (2014). Up till now, the couplings among the mechanical, magnetic and electric imperfections in the interfaces of piezomagnetic/piezoelectric composites have not been investigated. In the present paper, an interfacial imperfection coupling model (IICM) is proposed based on the magneto-electro-mechanical coupling phenomenon of the perfectly bonded interfacial region. It is an extended version of the GLSM and can degenerate to the GLSM just by supposing the coupling parameters to be zero. To demonstrate its applications, the IICM is further employed to perform in-plane facture analysis on a multiferroic composite consisting of a ferromagnetic layer and another ferroelectric layer.

In solving the problems of fracture mechanics, singular integral equations (SIEs) have been widely used since the early work of Muskhelishvili (1953a,b). Generally, when the dislocation density function (DDF) in the case of elastic materials (or the generalized DDF in the case of piezoelectric/piezomagnetic ceramics) is chosen as the auxiliary function, the boundary condition on the crack surface can be transformed into a Cauchy-type SIE (Zhou et al., 2010; Li et al., 2013). If the (generalized) dislocation function is instead taken as the auxiliary function, the crack-surface boundary condition can then be transformed into a hyper-singular integral equation (Choi, 1997; Zhu and Qin, 2007). For the crack problems with symmetry, the (generalized) displacement-slope function or the (generalized) displacement needs to be selected as the auxiliary function to derive the Cauchy-type SIE or the hyper-SIE (Chan et al., 2001a,b; Erdogan, 1985; Li et al., 2011; Li and Lee, 2010). The SIEs or hyper-SIEs of crack problems are typically constructed by the combined methods of integral transform and Green's functions, which require that the equivalent loading should be symmetrically applied on the crack surface (Mishuris et al., 2014). Apart from the Green's function based methods, the integral transform, Betti reciprocal theorem and weight functions can also be combined together to derive the SIEs (Morini et al., 2013; Piccolroaz and Mishuris, 2013; Mishuris et al., 2006). For example, Mishuris et al. (2014) derived the boundary integral formulation for a semi-infinite crack situated on an imperfect interface, on the basis of the weight function approach, the Betti reciprocal identity and integral transform. In the present paper, constant equivalent magneto-electro-mechanical loadings are applied on the crack surfaces. Therefore, the methods of integral transform and Green's functions are employed to derive the SIEs, from which the numerical solutions of the mechanical strain energy release rate are further obtained and the effects of the coupled interfacial imperfections on the fracture behavior are discussed and revealed.

2. Interfacial imperfection coupling model (IICM)

Due to the high temperature and pressure in the manufacture process of composites, inter-diffusion and permeation usually occur between different phases (Li and Lee, 2009). As a result, most practical composites have non-ignorable interfacial regions that consist of the atoms and/or molecules of different constituents. So, the interfacial regions may have not only the properties of the constituents but also some new performances. For example, the interfacial region between a ferromagnetic layer and another ferroelectric one is found to be a mixture of these two ingredients, which has the integrated magneto-electro-mechanical properties, including the piezomagnetic, piezoelectric and magneto-electric couplings (Zheng et al., 2004). Therefore, the interfacial region between the ferromagnetic and ferroelectric layers is actually a magneto-electro-mechanical medium. Assume that such an interfacial region is along the x-axis and polarized in its thickness direction, or, the z-axis. Then, for an interfacial region with no imperfection, the relation between the generalized stress and displacement can be formulated as (Huang and Kuo, 1997; Zhao and Fan, 2008)

$$\boldsymbol{\sigma}_z = \mathbf{M}\mathbf{u} \tag{4}$$

where the matrix $\mathbf{M}$ has the form

$$\mathbf{M} = \begin{bmatrix} c_{44}^{(0)}\partial_{,z} & c_{44}^{(0)}\partial_{,x} & h_{15}^{(0)}\partial_{,x} & e_{15}^{(0)}\partial_{,x}\\ c_{13}^{(0)}\partial_{,x} & c_{33}^{(0)}\partial_{,z} & h_{33}^{(0)}\partial_{,z} & e_{33}^{(0)}\partial_{,z}\\ h_{31}^{(0)}\partial_{,x} & h_{33}^{(0)}\partial_{,z} & -\mu_{33}^{(0)}\partial_{,z} & -d_{33}^{(0)}\partial_{,z}\\ e_{31}^{(0)}\partial_{,x} & e_{33}^{(0)}\partial_{,z} & -d_{33}^{(0)}\partial_{,z} & -\in_{33}^{(0)}\partial_{,z} \end{bmatrix} \tag{5}$$

where c, μ, $\in$, h, e and d are the elastic constant, magnetic permeability, dielectric coefficient, piezomagnetic coefficient, piezoelectric coefficient and magnetoelectric coefficient, respectively. In the subscripts, a coordinate following the comma denotes the partial derivative with respect to it.

Due to the abovementioned magneto-electro-mechanical couplings, it is possible that the magnetic, electric and mechanical imperfections cannot occur and grow independently in the interfacial regions between ferromagnetic and ferroelectric phases. In other words, the occurrence of any one of these three kinds of

interfacial imperfections may give rise to the other two ones. In addition, it is natural to infer that the coupling law among these three kinds of interfacial imperfections might be similar to that shown in Eqs. (4) and (5).

To derive the IICM, we also employ the jumps of the two mechanical displacements (u and w), the magnetic potential (φ) and the electric potential (φ) to represent the interfacial imperfections. Further, in the case of an infinitely long interfacial region, it is reasonable to assume that the generalized displacement only has transverse jump in the thickness direction (i.e., the z-axis direction). Under this assumption, it can be inferred from Eqs. (2)–(5) that the interfacial imperfections corresponding to the transverse jumps of w, φ and ϕ will be coupled together, but that associated with the transverse jump of u will be decoupled from them. Therefore, the generalized stiffness matrix $\mathbf{K}_\Gamma$ in Eq. (3) should be modified as

$$\mathbf{K}_\Gamma = \begin{bmatrix} \tilde{k}_\tau c_{44}^{(0)} & 0 & 0 & 0 \\ 0 & \tilde{k}_\sigma c_{33}^{(0)} & \tilde{k}_{\sigma B} h_{33}^{(0)} & \tilde{k}_{\sigma D} e_{33}^{(0)} \\ 0 & \tilde{k}_{\sigma B} h_{33}^{(0)} & -\tilde{k}_B \mu_{33}^{(0)} & -\tilde{k}_{BD} d_{33}^{(0)} \\ 0 & \tilde{k}_{\sigma D} e_{33}^{(0)} & -\tilde{k}_{BD} d_{33}^{(0)} & -\tilde{k}_D \in_{33}^{(0)} \end{bmatrix} \tag{6}$$

Combining Eqs. (2) and (6) together yields the IICM. Here, all the interfacial parameters $\tilde{k}_\tau$, $\tilde{k}_\sigma$, $\tilde{k}_B$, $\tilde{k}_D$, $\tilde{k}_{\sigma B}$, $\tilde{k}_{\sigma D}$ and $\tilde{k}_{BD}$ are non-negative and have the unified dimension of $[\text{length}]^{-1}$.

The four diagonal parameters $\tilde{k}_\tau$, $\tilde{k}_\sigma$, $\tilde{k}_B$ and $\tilde{k}_D$ represent the strength of the four interfacial imperfections, respectively. All of them have zero value when the interfacial region is not only mechanically debonded but also magnetically and electrically impermeable. They simultaneously go to infinity if the interface is perfectly bonded and meanwhile magnetically and electrically permeable. Any nonzero finite value of them corresponds to an intermediate state of the interfacial imperfections and a smaller value generally associates with a more serious imperfection. In addition, the three off-diagonal parameters $\tilde{k}_{\sigma B}$, $\tilde{k}_{\sigma D}$ and $\tilde{k}_{BD}$ represent the strength of the intercouplings among the three kinds of interfacial imperfections, respectively. Larger values of them generally correspond to stronger couplings.

The existence of interfacial imperfections and their couplings will necessarily affect the mechanical behaviors of the composites. Next, as an example, the IICM is applied to the fracture problem of a multiferroic composite and its effect on the intra-layer fracture behavior is surveyed.

3. Application to a fracture problem

3.1. Problem formulation

Fig. 1 shows the facture model of a multiferroic composite that consists of a ferromagnetic layer, a ferroelectric layer and an intermediate imperfect interfacial region. The thickness of the interfacial region is h_0 and those of the two layers are $h_1 - h_0$ and h_2. For the purpose of comparison, it is assumed that there are two groups of cracks, parallel to the interfacial region and each in a layer. Set a Cartesian coordinate system with the rightward x-axis along the lower interface of the interfacial region and the upward z-axis along the direction of thickness. Then, the locations of the two crack groups are denoted by $z_{\text{I}} = h_{\text{I}}$ and $z_{\text{II}} = -h_{\text{II}}$. As shown in Fig. 1, the quantities of the interfacial region and the ferromagnetic and ferroelectric layers are identified by subscripts/superscripts 0, 1 and 2, respectively. Those associated with the two crack groups are instead marked by subscripts/superscripts I and II.

Assume that the composite is polarized along the z-axis. Then, the basic equations of the ferromagnetic and ferroelectric layers have the form (Huang and Kuo, 1997)

$$\left.\begin{aligned} &\sigma_{x,x}^{(i)} + \tau_{xz,z}^{(i)} = 0; \quad \tau_{zx,x}^{(i)} + \sigma_{z,z}^{(i)} = 0 \\ &B_{x,x}^{(i)} + B_{z,z}^{(i)} = 0; \quad D_{x,x}^{(i)} + D_{z,z}^{(i)} = 0 \end{aligned}\right\}, \quad (i = 1, 2) \tag{7}$$

$$\left.\begin{aligned} \sigma_x^{(i)} &= c_{11}^{(i)} u_{i,x} + c_{13}^{(i)} w_{i,z} + \delta_{1i} h_{31} \varphi_{i,z} + \delta_{2i} e_{31} \phi_{i,z} \\ \sigma_z^{(i)} &= c_{13}^{(i)} u_{i,x} + c_{33}^{(i)} w_{i,z} + \delta_{1i} h_{33} \varphi_{i,z} + \delta_{2i} e_{33} \phi_{i,z} \\ \tau_{zx}^{(i)} &= c_{44}^{(i)} (u_{i,z} + w_{i,x}) + \delta_{1i} h_{15} \varphi_{i,x} + \delta_{2i} e_{15} \phi_{i,x} \\ B_x^{(i)} &= \delta_{1i} h_{15} (u_{i,z} + w_{i,x}) - \mu_{11}^{(i)} \varphi_{i,x} \\ B_z^{(i)} &= \delta_{1i} (h_{31} u_{i,x} + h_{33} w_{i,z}) - \mu_{33}^{(i)} \varphi_{i,z} \\ D_x^{(i)} &= \delta_{2i} e_{15} (u_{i,z} + w_{i,x}) - \varepsilon_{11}^{(i)} \phi_{i,x} \\ D_z^{(i)} &= \delta_{2i} (e_{31} u_{i,x} + e_{33} w_{i,z}) - \varepsilon_{33}^{(i)} \phi_{i,z} \end{aligned}\right\}, \quad (i = 1,\ 2) \tag{8}$$

where δ_{ji} $(j = 1, 2)$ is the Kronecker sign that is 1 when its two subscripts are identical and 0 otherwise.

Assume that the imperfect interfacial region comply with the IICM. Then, the boundary and continuity conditions of the fracture problem in Fig. 1 can be stated as

$$\boldsymbol{\sigma}_z(x, h_1) = \mathbf{0}; \quad \boldsymbol{\sigma}_z(x, -h_2) = \mathbf{0} \tag{9}$$

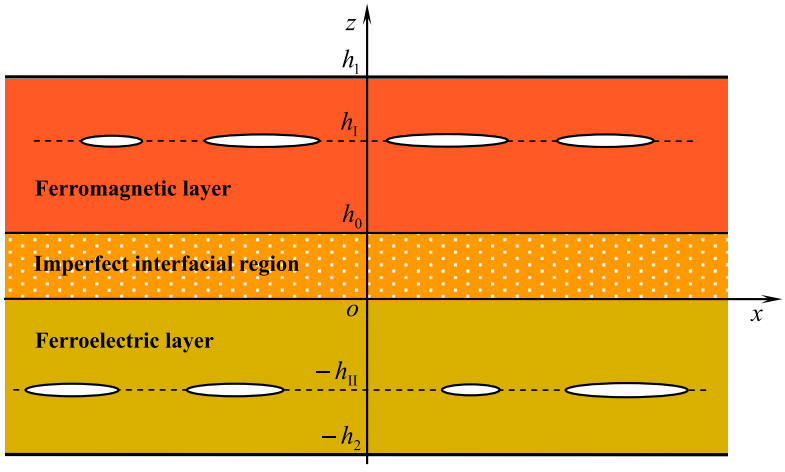

Fig. 1. The fracture model of a multiferroic composite containing an imperfect interfacial region.

$$\boldsymbol{\sigma}_z(x,h_0)=\boldsymbol{\sigma}_z(x,0) \tag{10}$$

$$\boldsymbol{\sigma}_z(x,0)=\mathbf{K}_\Gamma[\mathbf{u}(x,h_0)-\mathbf{u}(x,0)] \tag{11}$$

$$\boldsymbol{\sigma}_z(x,z_k^+)=\boldsymbol{\sigma}_z(x,z_k^-) \tag{12}$$

$$\mathbf{u}(x,z_k^+)=\mathbf{u}(x,z_k^-),\quad x\notin\bigcup_{i=1}^{n_k}\left(a_i^{(k)},b_i^{(k)}\right) \tag{13}$$

$$\boldsymbol{\sigma}_z(x,z_k)=-\boldsymbol{\sigma}_k,x\in\bigcup_{i=1}^{n_k}\left(a_i^{(k)},b_i^{(k)}\right) \tag{14}$$

where $k=\mathrm{I},\mathrm{II}$. $\mathbf{K}_\Gamma$ is given in Eq. (6). $-\boldsymbol{\sigma}_k$ is the equivalent generalized traction on the crack surfaces. n_I and n_II are the crack amounts of the two crack groups. $(a_i^{(k)},b_i^{(k)})$ is the x-interval occupied by the ith crack.

3.2. Fracture analysis

3.2.1. Generalized dislocation simulation

To solve the fracture problem, two groups of continuously distributed generalized dislocations (CDGDs) are used to simulate the cracks, whose density functions are defined as

$$\mathbf{g}_i^{(k)}(x)=\begin{cases}\mathbf{u}_{,x}(x,z_k^+)-\mathbf{u}_{,x}(x,z_k^-), & x\in\bigcup_{i=1}^{n_k}\left(a_i^{(k)},b_i^{(k)}\right)\\ 0, & x\notin\bigcup_{i=1}^{n_k}(a_i^{(k)},b_i^{(k)})\end{cases} \tag{15}$$

where $k=\mathrm{I},\mathrm{II}$ and $\mathbf{g}=\begin{bmatrix}g_u & g_w & g_\varphi & g_\phi\end{bmatrix}^{\mathrm{T}}$. Obviously, Eq. (13) is automatically satisfied. To solve the problems of the two groups of CDGDs, one needs to get the Green's functions of the generalized stress field (GSF) induced by two generalized point dislocations (GPDs) that are defined as

$$\mathbf{u}_{,x}(x,z_k^+)-\mathbf{u}_{,x}(x,z_k^-)=\delta(x-s_k)\mathbf{g}_k(s_k),\quad (k=\mathrm{I},\mathrm{II}) \tag{16}$$

where s_I and s_II are the abscissas of the two GPDs, and $\mathbf{g}_\mathrm{I}(s_\mathrm{I})$ and $\mathbf{g}_\mathrm{II}(s_\mathrm{II})$ are their amplitudes. δ is the Dirac delta function.

3.2.2. Singular integral equations (SIEs)

Because the Dirac delta function can be expressed as an even function plus an odd one, the generalized displacement field (GDF) induced by a GPD can be divided into a symmetric part and an anti-symmetric one (Li et al., 2011, 2013). Substituting Eq. (8) into Eq. (7) and applying Fourier integral transform to the resulting governing equations, one can obtain the solutions of the GDF (Li et al., 2011). Based on Eqs. (9), (10), (11), (12) and (16), the undetermined coefficients of GDF can be expressed as functions of $\mathbf{g}_\mathrm{I}(s_\mathrm{I})$ and $\mathbf{g}_\mathrm{II}(s_\mathrm{II})$. Then, the Green's functions of GSF can be determined. Finally, according to the theory of Green's function and the CDGDs defined in Eqs. (15), Eq. (14) can be transformed into a system of SIEs (Li et al., 2011, 2013)

$$\left.\begin{aligned}&\frac{1}{\pi}\sum_{i=1}^{n_\mathrm{I}}\int_{-1}^{1}\left[\frac{a_{0i}^{(\mathrm{I})}}{a_{0l}^{(\mathrm{I})}\tilde{x}_l^{(\mathrm{I})}+c_{0l}^{(\mathrm{I})}-a_{0i}^{(\mathrm{I})}\tilde{s}_i^{(\mathrm{I})}-c_{0i}^{(\mathrm{I})}}\mathbf{q}_\mathrm{I}+\tilde{\mathbf{R}}^{(\mathrm{I}1)}\left(\tilde{s}_i^{(\mathrm{I})},\tilde{x}_l^{(\mathrm{I})}\right)\right]\tilde{\mathbf{g}}_i^{(\mathrm{I})}\left(\tilde{s}_i^{(\mathrm{I})}\right)\mathrm{d}\tilde{s}_i^{(\mathrm{I})}\\&\quad+\frac{1}{\pi}\sum_{j=1}^{n_\mathrm{II}}\int_{-1}^{1}\tilde{\mathbf{R}}^{(\mathrm{II}1)}\left(\tilde{s}_j^{(\mathrm{II})},\tilde{x}_l^{(\mathrm{I})}\right)\tilde{\mathbf{g}}_j^{(\mathrm{II})}\left(\tilde{s}_j^{(\mathrm{II})}\right)\mathrm{d}\tilde{s}_j^{(\mathrm{II})}=-\boldsymbol{\sigma}_\mathrm{I}\\&\frac{1}{\pi}\sum_{j=1}^{n_\mathrm{II}}\int_{-1}^{1}\left[\frac{a_{0j}^{(\mathrm{II})}}{a_{0m}^{(\mathrm{II})}\tilde{x}_m^{(\mathrm{II})}+c_{0m}^{(\mathrm{II})}-a_{0j}^{(\mathrm{II})}\tilde{s}_j^{(\mathrm{II})}-c_{0j}^{(\mathrm{II})}}\mathbf{q}_\mathrm{II}+\tilde{\mathbf{R}}^{(\mathrm{II}2)}\left(\tilde{s}_j^{(\mathrm{II})},\tilde{x}_m^{(\mathrm{II})}\right)\right]\tilde{\mathbf{g}}_j^{(\mathrm{II})}\left(\tilde{s}_j^{(\mathrm{II})}\right)\mathrm{d}\tilde{s}_j^{(\mathrm{II})}\\&\quad+\frac{1}{\pi}\sum_{i=1}^{n_\mathrm{I}}\int_{-1}^{1}\tilde{\mathbf{R}}^{(\mathrm{I}2)}\left(\tilde{s}_i^{(\mathrm{I})},\tilde{x}_m^{(\mathrm{II})}\right)\tilde{\mathbf{g}}_i^{(\mathrm{I})}\left(\tilde{s}_i^{(\mathrm{I})}\right)\mathrm{d}\tilde{s}_i^{(\mathrm{I})}=-\boldsymbol{\sigma}_\mathrm{II}\end{aligned}\right\} \tag{17}$$

where $l=1,2,\ldots,n_\mathrm{I}$ and $m=1,2,\ldots,n_\mathrm{II}$. $\tilde{\mathbf{R}}^{(\mathrm{I}1)}\left(\tilde{s}_i^{(\mathrm{I})},\tilde{x}_l^{(\mathrm{I})}\right)$, $\tilde{\mathbf{R}}^{(\mathrm{II}1)}\left(\tilde{s}_j^{(\mathrm{II})},\tilde{x}_l^{(\mathrm{I})}\right)$, $\tilde{\mathbf{R}}^{(\mathrm{II}2)}\left(\tilde{s}_j^{(\mathrm{II})},\tilde{x}_m^{(\mathrm{II})}\right)$ and $\tilde{\mathbf{R}}^{(\mathrm{I}2)}\left(\tilde{s}_i^{(\mathrm{I})},\tilde{x}_m^{(\mathrm{II})}\right)$ are kernel-function matrices. $\mathbf{q}_\mathrm{I}$ and $\mathbf{q}_\mathrm{II}$ are constant matrices depending on the material constants. They are given in Appendix A. $a_{0p}^{(k)}$ and $c_{0p}^{(k)}$ $(p=1,2,\ldots,n_k;\ k=\mathrm{I},\mathrm{II})$ are the half length and central abscissa of the pth crack. $\tilde{s}_p^{(k)}=(s_p^{(k)}-c_{0p}^{(k)})/a_{0p}^{(k)}\in(-1,1)$ and $\tilde{x}_p^{(k)}=(x_p^{(k)}-c_{0p}^{(k)})/a_{0p}^{(k)}\in(-1,1)$ $(p=1,2,\ldots,n_k;\quad k=\mathrm{I},\mathrm{II})$. $\tilde{\mathbf{g}}_p^{(k)}\left(\tilde{s}_p^{(k)}\right)=\mathbf{g}_p^{(k)}\left(a_{0p}^{(k)}\tilde{s}_p^{(k)}+c_{0p}^{(k)}\right)$ $(p=1,2,\ldots,n_k;k=\mathrm{I},\mathrm{II})$.

Introduce two groups of new function vectors

$$\mathbf{f}_i^{(k)}\left(\tilde{s}_i^{(k)}\right)=\tilde{\mathbf{g}}_i^{(k)}\left(\tilde{s}_i^{(k)}\right)\sqrt{1-\left[\tilde{s}_i^{(k)}\right]^2},\quad (i=1,2,\ldots,n_k;\quad k=\mathrm{I},\mathrm{II}) \tag{18}$$

Then, using the method of Lobatto–Chebyshev collocation, the SIEs in Eq. (17) and the single-value conditions can be transformed into a system of algebraic equations (Erdogan and Gupta, 1972; Theocaris and Ioakimids, 1977), from which the numerical solutions of the new function vectors in Eq. (18) can be obtained.

3.2.3. Mechanical strain energy release rate (MSERR)

In the cases of in-plane fracture in piezomagnetic/piezoelectric materials, the mechanical strain energy release rate (MSERR) G_m is generally a preferred fracture parameter (Park and Sun, 1995). For the present I-II mixed mode fracture problem, the MSERRs of the left and right tips of each crack are given by (Li et al., 2013; Zhong and Lee, 2011)

$$G_\mathrm{m}^{(j)}=0.5\left[K_\sigma^{(j)}K_\mathrm{COD}^{(j)}+K_\tau^{(j)}K_\mathrm{CSD}^{(j)}\right] \tag{19}$$

where the superscript j is the identifier of each crack tip, i.e., it is $a_i^{(k)}$ or $b_i^{(k)}$ $(i=1,2,\ldots,n_k;\ k=\mathrm{I},\mathrm{II})$. K_σ, K_τ, K_COD and K_CSD are the intensity factors of normal stress, shear stress, crack opening displacement and crack shear displacement, respectively. They can be determined from the numerical solutions of the following generalized intensity factors

$$\left.\begin{aligned}\mathbf{K}_\tau^{(a_i^{(k)})}&=-\mathbf{q}_k^{(w)}\mathbf{f}_i^{(k)}(-1)\sqrt{\pi a_{0i}^{(k)}}\\ \mathbf{K}_\tau^{(b_i^{(k)})}&=\mathbf{q}_k^{(w)}\mathbf{f}_i^{(k)}(1)\sqrt{\pi a_{0i}^{(k)}}\\ \mathbf{K}_w^{(a_i^{(k)})}&=0.5\mathbf{f}_{iw}^{(k)}(-1)\sqrt{\pi a_{0i}^{(k)}}\\ \mathbf{K}_w^{(b_i^{(k)})}&=-0.5\mathbf{f}_{iw}^{(k)}(1)\sqrt{\pi a_{0i}^{(k)}}\end{aligned}\right\},\quad (i=1,2,\ldots,n_k;k=\mathrm{I},\mathrm{II}) \tag{20}$$

where $\mathbf{K}_\tau=\begin{bmatrix}K_\tau & K_\sigma\end{bmatrix}^{\mathrm{T}}$ and $\mathbf{K}_w=\begin{bmatrix}K_\mathrm{CSD} & K_\mathrm{COD}\end{bmatrix}^{\mathrm{T}}$. $\mathbf{q}_k^{(w)}$ is a sub-matrix consisting of the first and second rows of $\mathbf{q}_k$. $\mathbf{f}_{iw}^{(k)}$ is a sub-vector consisting of the first and second elements of $\mathbf{f}_i^{(k)}$.

4. Numerical results and discussion

Numerical results of MSERR are provided to survey the effects of the coupled interfacial imperfections on the fracture behavior of the composite. The ferromagnetic and ferroelectric phases are assumed to be $CoFe_2O_4$ and $BaTiO_3$ (Zheng et al., 2004), whose properties are shown in Tables 1 and 2 (Xue and Liu, 2010). In addition, the magneto-electro-elastic properties of the perfect interfacial region are given in Table 3 (Zhong et al., 2009b).

To simplify the numerical calculation and focus our attention on studying the effects of the interfacial imperfections, each groups of cracks are reduced to be a single one. As shown in Fig. 2, the two cracks have identical distance off the interfacial region, which is denoted by d, i.e., $h_\mathrm{I}-h_0=h_\mathrm{II}=d$. $(a_\mathrm{I},b_\mathrm{I})$ and $(a_\mathrm{II},b_\mathrm{II})$ are the x-intervals occupied by the two cracks, while $a_0^{(\mathrm{I})}$ and $c_0^{(\mathrm{I})}$ $(k=\mathrm{I},\mathrm{II})$ represent their half lengths and central abscissas. The horizontal space between the two crack centers is denoted by d_c, i.e., $d_c=|c_0^{(\mathrm{I})}-c_0^{(\mathrm{II})}|$. It deserves noting that when $a_0^{(\mathrm{I})}$, $a_0^{(\mathrm{II})}$ and d_c are

Table 1
Properties of $CoFe_2O_4$ (Xue and Liu, 2010).

$c_{11}^{(1)}$	$c_{13}^{(1)}$	$c_{33}^{(1)}$	$c_{44}^{(1)}$	h_{31}	h_{33}	h_{15}	$\varepsilon_{11}^{(1)}$	$\varepsilon_{33}^{(1)}$	$\mu_{11}^{(1)}$	$\mu_{33}^{(1)}$
10^9 N/m^2				N/(Am)			10^{-9} C^2/(Nm^2)		10^{-6} Ns^2/C^2	
286	170.5	269.5	45.3	580.3	699.7	550	0.08	0.093	157	157

Table 2
Properties of $BaTiO_3$ (Xue and Liu, 2010).

$c_{11}^{(2)}$	$c_{13}^{(2)}$	$c_{33}^{(2)}$	$c_{44}^{(2)}$	e_{31}	e_{33}	e_{15}	$\varepsilon_{11}^{(2)}$	$\varepsilon_{33}^{(2)}$	$\mu_{11}^{(2)}$	$\mu_{33}^{(2)}$
10^9 N/m^2				C/m^2			10^{-9} C^2/(Nm^2)		10^{-6} Ns^2/C^2	
166	78	162	43	−4.4	18.6	11.6	11.2	12.6	5	10

Table 3
The properties of the perfect interfacial region (Zhong et al., 2009b).

$c_{33}^{(0)}$	$c_{44}^{(0)}$	$e_{33}^{(0)}$	$h_{33}^{(0)}$	$\in_{33}^{(0)}$	$\mu_{33}^{(0)}$	$d_{33}^{(0)}$
10^9N/m^2		C/m^2	N/(Am)	10^{-9}C^2/(Nm^2)	10^{-4}Ns^2/C^2	10^{-12}NsV^{-1}C^{-1}
216	44	9.3	350	6.35	0.835	2737.5

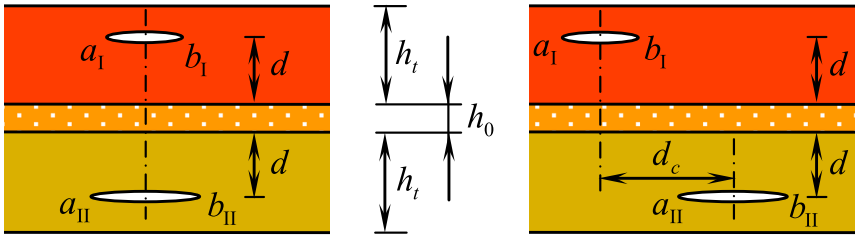

(a) The coaxial case (b) The un-coaxial case

Fig. 2. The simplified fracture model.

specified, the MSERR is independent of the specific values of $c_0^{(I)}$ and $c_0^{(II)}$ because the composite is infinitely long. In addition, both the ferromagnetic and ferroelectric layers have the same thickness of 50 mm, i.e., h_t = 50 mm, and the thickness of the interfacial region is set as 0.05 mm, i.e., h_0 = 0.05 mm.

The two cracks are assumed to have the same equivalent loadings on their surfaces, that is to say, $\boldsymbol{\sigma}_I = \boldsymbol{\sigma}_{II} = \boldsymbol{\sigma}_0 = [\tau_0 \quad \sigma_0 \quad B_0 \quad D_0]^T$. The equivalent loadings are given in the following way (Li et al., 2013)

$$\tau_0 = \lambda_\tau \sigma_0; \quad B_0 = \lambda_B \sigma_0 h_{33}/c_{33}^{(1)}; \quad D_0 = \lambda_D \sigma_0 e_{33}/c_{33}^{(2)} \tag{21}$$

where λ_τ, λ_B and λ_D are the dimensionless loading factors of shear stress, magnetic induction and electric displacement (Li and Lee, 2010), respectively. In subsequent computations, σ_0 is 5 MPa and the loading factors are $\lambda_\tau = 0$ and $\lambda_B = \lambda_D = 2$.

4.1. Convergence behaviors of kernel functions

In order to control the computation efficiency and accuracy, the convergence behaviors of the kernel functions in Eq. (17) should be surveyed at first. It is seen from the appendix that they have the form of infinite integrals. In calculation, the infinite integral interval $[0, +\infty)$ is truncated as a finite one $[0, N]$, whose upper limit N is to be determined based on the convergence speed of the kernel functions and the requirement of computation accuracy. There are 64 kernel functions in Eq. (17), and computation indicates that all of them have similar convergence speed. Taking four of them as examples, Fig. 3 shows their convergence behaviors. It is found that the convergence speed mainly depends on the normalized distance d/h_t. Generally, the convergence speed decreases remarkably if d/h_t goes to 0 or 1.0. In the following computation, the convergence accuracy of the kernel functions is specified as 1.0×10^{-4}, and N is changed adaptively with d/h_t. For example, if $d/h_t = 0.02$, N can be given as 10,000 m^{-1} to guarantee the convergence accuracy of 1.0×10^{-4}; if $d/h_t = 0.1$, N can be instead determined as 5000 m^{-1}.

4.2. Verification

The intra-layer fracture behavior has been investigated by Li et al. (2013) on a piezomagnetic/piezoelectric bi-material with two cracks parallel to the perfect interface and each in a layer. An example is taken from there to verify the present numerical results. As indicated by Eqs. (2) and (6), when $\tilde{k}_{\sigma B} = \tilde{k}_{\sigma D} = \tilde{k}_{BD}$ = 0 m^{-1} and all the other four interface parameters (i.e., $\tilde{k}_\tau$, $\tilde{k}_\sigma$, $\tilde{k}_B$ and $\tilde{k}_D$) have enough large values, the coupled imperfect interfacial region will become a perfectly bonded and meanwhile magnetically and electrically permeable interface. Under this condition, the case shown in Fig. 2(b) of Li et al. (2013) can be reproduced just by further assuming that $a_0^{(I)} = a_0^{(II)}$ = 1 mm and d_c = 0 mm. The present results are compared with those of Li et al. (2013) in Fig. 4(a), where $\tilde{k}_\tau$, $\tilde{k}_\sigma$, $\tilde{k}_B$ and $\tilde{k}_D$ are supposed to be identical just for simplicity. Four values of them, i.e., 0 m^{-1}, 100 m^{-1}, 500 m^{-1} and 10,000 m^{-1}, are used to make

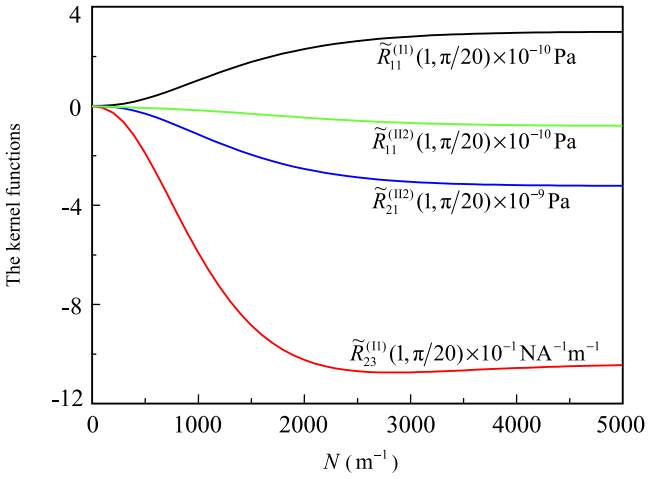

(a) d/h_t =0.02

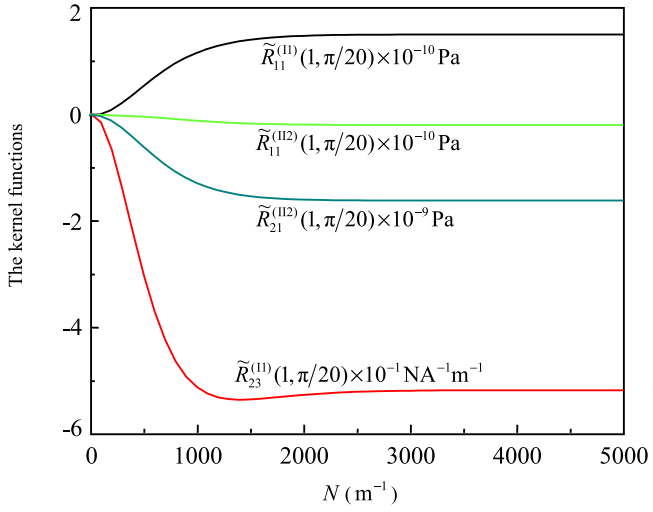

(b) d/h_t =0.04

Fig. 3. The convergence behavior of the kernel functions in the coaxial case. ($\tilde{k}_\tau = \tilde{k}_\sigma = \tilde{k}_B = \tilde{k}_D = \tilde{k}_{\sigma B} = \tilde{k}_{\sigma D} = \tilde{k}_{BD} = 0$ m^{-1}).

the comparison. When $\tilde{k}_\tau = \tilde{k}_\sigma = \tilde{k}_B = \tilde{k}_D = 10,000$ m^{-1}, the present results agree well with those of Li et al. (2013), verifying the validity of the numerical computation here. In addition, some other remarks still need to make:

- When $\tilde{k}_\tau$, $\tilde{k}_\sigma$, $\tilde{k}_B$ and $\tilde{k}_D$ have the other three values, i.e., 0 m^{-1}, 10 m^{-1}, and 500 m^{-1}, the present results do not agree with those of Li et al. (2013) but their differences only occur in the region of $d/h_t < 0.4$. On one hand, this implies that when the four interfacial parameters have these small values, the interface will be imperfect, leading to the differences of the results. On the other hand, it indicates that the interfacial imperfections only affect the cracks in the region of $d/h_t < 0.4$. In addition, the affected range of the imperfect interface is an interesting topic also surveyed by Li and Lee (2009). In their study, a crack is inclined to the imperfect interface in a piezoelectric composite (see Fig. 4(b)), and the generalized spring-type model is adopted to formulate the interfacial imperfections. In Section 4.2.2 of Li and Lee (2009), h_p/a_0 is fixed as 5.0 and it was found that the imperfect interface may affect the crack tip-a when $0 < h_0 \leqslant 2a_0$. Referring to Fig. 4(b), one can found that

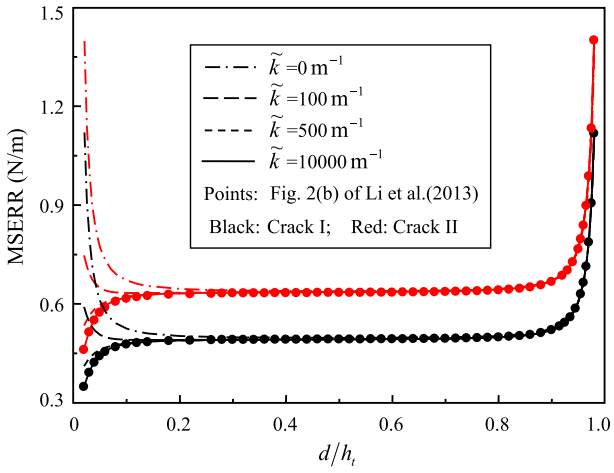

(a) Effect of the transverse positional parameter of two coaxial and equal cracks on MSERR

($a_0^{(I)} = a_0^{(II)} = 1$mm; $d_c = 0$mm; $\widetilde{k}_\tau = \widetilde{k}_\sigma = \widetilde{k}_B = \widetilde{k}_D = \widetilde{k}$; $\widetilde{k}_{\sigma B} = \widetilde{k}_{\sigma D} = \widetilde{k}_{BD} = 0$ m^{-1})

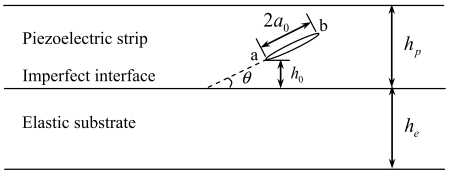

(b) An existing model studied by Li and Lee (2009)

Fig. 4. Numerical verification.

$0 < h_0 \leqslant 2a_0$ is equivalent to $0 < h_0/h_p \leqslant 0.4$. Therefore, the above conclusion of the present paper agrees with the corresponding result of Li and Lee (2009). However, it deserves noting that the above conclusion only holds true for the specific case in Fig. 4(a), where $\tilde{k}_\tau = \tilde{k}_\sigma = \tilde{k}_B = \tilde{k}_D = \tilde{k}$, $\tilde{k}_{\sigma B} = \tilde{k}_{\sigma D} = \tilde{k}_{BD} = 0$ m^{-1}, $a_0^{(I)} = a_0^{(II)} = 1$ mm; $d_c = 0$ mm, $h_t = 50$ mm and $h_0 = 0.05$ mm. The affected range of the imperfect interface may be different in the more general case.

- When $\tilde{k}_\tau$, $\tilde{k}_\sigma$, $\tilde{k}_B$ and $\tilde{k}_D$ have values of 0 m^{-1} and 100 m^{-1}, the MSERR goes up steeply as $d/h_t \to 0$, which is the same as its behavior in the neighboring region of the free surface (i.e., $d/h_t \to 1.0$). This is because the value of 100 m^{-1} or even 0 m^{-1} corresponds to so small a generalized interfacial stiffness that the imperfect interface acts like a free surface, which generally makes the MSERR of an approaching crack go up obviously. In addition, as revealed by Li et al. (2013), when two coaxial parallel cracks of equal length approach each other, a shielding effect can be observed, i.e., their MSERRs go down, even if there is a perfect interface in between. Here, the shooting up of the MSERR indicates that the interaction between the two parallel cracks is prevented by the intermediate imperfect interface with enough small generalized interfacial stiffness.
- When $\tilde{k}_\tau$, $\tilde{k}_\sigma$, $\tilde{k}_B$ and $\tilde{k}_D$ have values of 500 m^{-1} and 10,000 m^{-1}, the MSERR goes down slightly as $d/h_t \to 0$. This is because the value of 500 m^{-1} or even 10,000 m^{-1} corresponds to so large a generalized interfacial stiffness that the imperfect interface cannot completely cancel the shielding effect between the two parallel cracks.

4.3. Effects of interfacial imperfections and their couplings

The interactions including shielding and interference can occur between two parallel cracks when they are near to each other, even if there is an interface in between (Li et al., 2013). To focus on

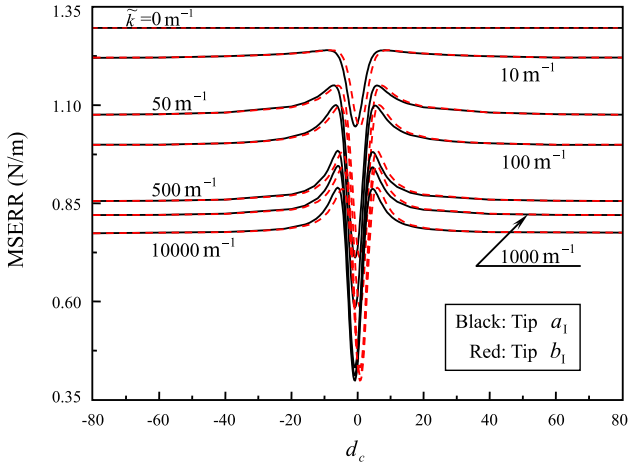

(a) MSERR of crack I

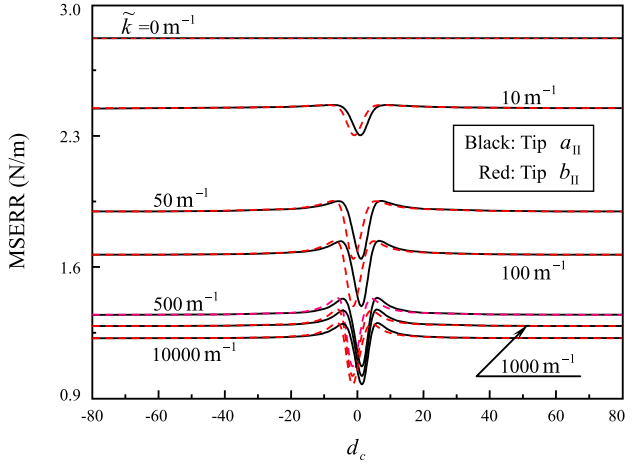

(b) MSERR of crack II

Fig. 5. Effect of the horizontal space on MSERR. ($a_0^{(\mathrm{I})}$ = 1.5 mm; $a_0^{(\mathrm{II})}$ = 2 mm; d = 2 mm; $\tilde{k}_\tau = \tilde{k}_\sigma = \tilde{k}_B = \tilde{k}_D = \tilde{k}$; $\tilde{k}_{\sigma B} = \tilde{k}_{\sigma D} = \tilde{k}_{BD} = 0$ m^{-1}).

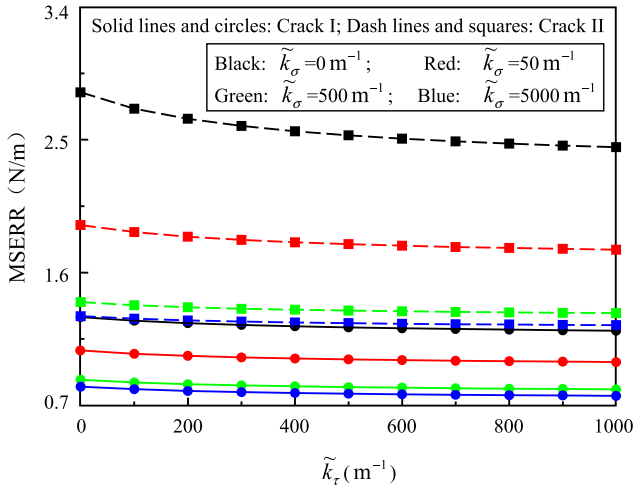

(a) Effect of $\tilde{k}_\tau$

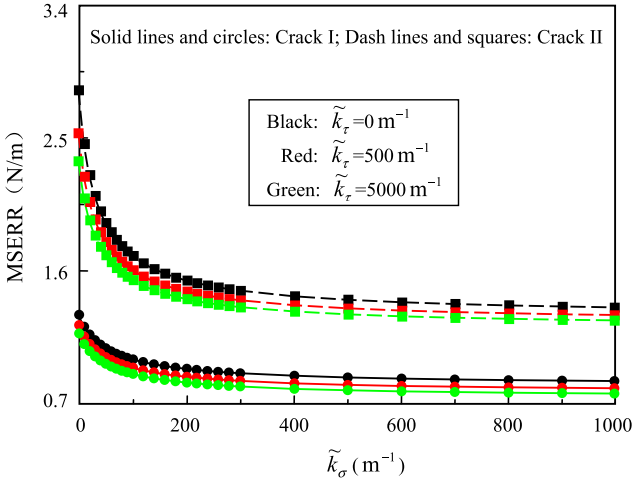

(b) Effect of $\tilde{k}_\sigma$

Fig. 6. Effects of mechanical imperfections on MSERR. ($a_0^{(\mathrm{I})}$ = 1.5 mm; $a_0^{(\mathrm{II})}$ = 2 mm; d = 2 mm; d_c = 100 mm; $\tilde{k}_B = \tilde{k}_D = \tilde{k}_{\sigma B} = \tilde{k}_{\sigma D} = \tilde{k}_{BD} = 0$ m^{-1}).

investigating the effects of interfacial imperfections and their couplings, it is better to avoid such interactions. For this purpose, it is assumed in this section that the two cracks are un-coaxial (see Fig. 2(b)) and their horizontal space d_c is large enough to eliminate their interactions. Therefore, a suitable value of d_c should be chosen at first. Due to this reason, the effect of d_c on MSERR is surveyed in Fig. 5. It is seen that there is no interaction between the two cracks when the interface is mechanically debonded and magnetically and electrically impermeable (i.e., $\tilde{k}_\tau = \tilde{k}_\sigma = \tilde{k}_B = \tilde{k}_D = 0$ m^{-1}). However, if the interface is just partially imperfect or even has no imperfection (i.e., $\tilde{k}_\tau$, $\tilde{k}_\sigma$, $\tilde{k}_B$ and $\tilde{k}_D$ are larger than 0 m^{-1} or even tend to infinity), interactions between the two cracks may occur, leading to obvious local oscillation of MSERR (Li et al., 2013). In the case of d = 2 mm, $a_0^{(\mathrm{I})}$ = 1.5 mm and $a_0^{(\mathrm{II})}$ = 2 mm, it is seen that a horizontal space of not less than 80 mm is large enough to avoid the crack interactions. In subsequent computation, d, $a_0^{(\mathrm{I})}$ and $a_0^{(\mathrm{II})}$ keep the same values as those in Fig. 5 and d_c is set as 100 mm to assure the elimination of the crack interactions. Under this condition, the two tips of each crack always have identical MSERRs.

4.3.1. Effects of mechanical imperfections

The present problem involves two kinds of mechanical interfacial imperfections, one along the thickness direction and characterized by $\tilde{k}_\sigma$, and the other along the longitudinal direction and described by $\tilde{k}_\tau$. Their effects on MSERR are illustrated in Fig. 6. As these two mechanical imperfection parameters decrease to 0 m^{-1} (i.e., the interfacial region becomes mechanically imperfect and even debonded), MSERR goes up, showing an effect like that of a free surface.

In addition, comparison between Fig. 6(a) and (b) indicates that the effect of $\tilde{k}_\sigma$ is much more prominent than that of $\tilde{k}_\tau$. Therefore, $\tilde{k}_\sigma$ is the dominant parameter of the two mechanical imperfections. Moreover, its dominance is still embodied by the fact that whether $\tilde{k}_\tau$ can affect MSERR or not depends on the magnitude of $\tilde{k}_\sigma$. If $\tilde{k}_\sigma$ is 0 m^{-1}, $\tilde{k}_\tau$ will has its maximum effect on MSERR; however, when $\tilde{k}_\sigma$ has enough large value such as 5000 m^{-1}, the effect of $\tilde{k}_\tau$ will become vanishingly small. The dominance of $\tilde{k}_\sigma$ over $\tilde{k}_\tau$ demonstrates that in engineering we should focus on monitoring the transverse mechanical interfacial imperfection rather than the longitudinal one.

4.3.2. Effect of magnetic imperfection

The curves of MSERR versus the magnetic imperfection parameter $\tilde{k}_B$ is shown in Fig. 7 with the magneto-mechanical

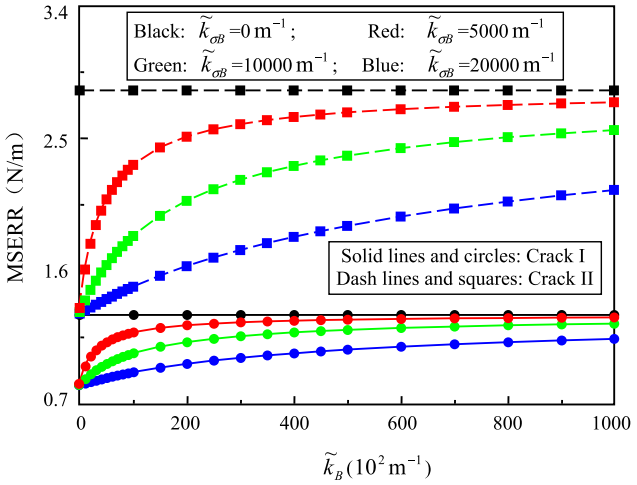

Fig. 7. Effect of magnetic imperfection on MSERR. ($a_0^{(\mathrm{I})}$ = 1.5 mm; $a_0^{(\mathrm{II})}$ = 2 mm; d = 2 mm; d_c = 100 mm; $\tilde{k}_\tau=\tilde{k}_\sigma=\tilde{k}_D=\tilde{k}_{\sigma D}=\tilde{k}_{BD}=0\ \mathrm{m}^{-1}$).

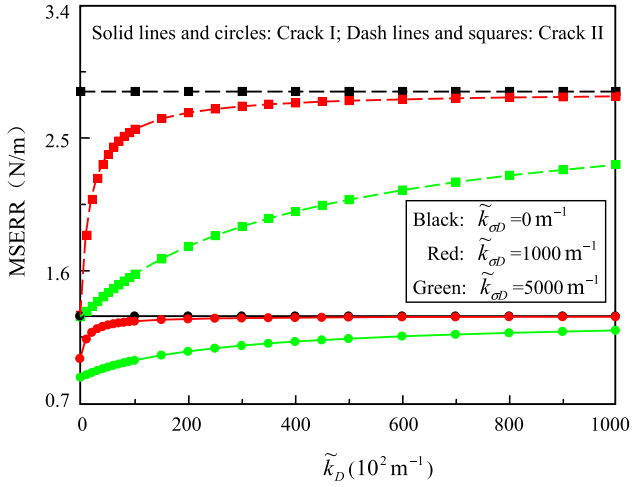

Fig. 8. Effect of electric imperfection on MSERR. ($a_0^{(\mathrm{I})}$ = 1.5 mm; $a_0^{(\mathrm{II})}$ = 2 mm; d = 2 mm; d_c = 100 mm; $\tilde{k}_\tau=\tilde{k}_\sigma=\tilde{k}_B=\tilde{k}_{\sigma B}=\tilde{k}_{BD}=0\ \mathrm{m}^{-1}$).

imperfection coupling parameter $\tilde{k}_{\sigma B}$ varying among four values of 0 m^{-1}, 5000 m^{-1}, 10,000 m^{-1} and 20,000 m^{-1}. When $\tilde{k}_{\sigma B}=0\ \mathrm{m}^{-1}$, MSERR never changes with the varying $\tilde{k}_B$. However, in the case of nonzero $\tilde{k}_{\sigma B}$, as $\tilde{k}_B$ increases from 0 m^{-1}, MSERR goes up and gradually converges to its value in the case of zero $\tilde{k}_{\sigma B}$. Therefore, whether the magnetic imperfection affects MSERR or not depends on the magneto-mechanical imperfection coupling. If there is no coupling, the magnetic imperfection has no effect on MSERR; if such coupling exists, the magnetic imperfection can lower down MSERR. Generally, more serious magnetic imperfection (i.e., smaller $\tilde{k}_B$) plus stronger magneto-mechanical imperfection coupling (i.e., larger $\tilde{k}_{\sigma B}$) will give rise to smaller MSERR. Therefore, when studying the magnetic imperfection, we should not neglect the magneto-mechanical imperfection coupling.

4.3.3. Effect of electric imperfection

Fig. 8 displays the curves of MSERR versus the electric imperfection parameter $\tilde{k}_D$ with the electro-mechanical imperfection coupling parameter $\tilde{k}_{\sigma D}$ changing among three values including 0 m^{-1}, 1000 m^{-1} and 5000 m^{-1}. Like in the case of magnetic imperfection, the effect of electric imperfection on MSERR depends on

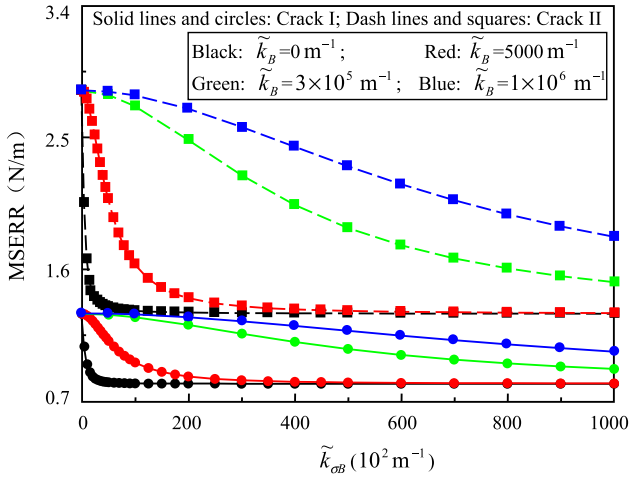

Fig. 9. Effect of magnetic and mechanical imperfection coupling on MSERR. ($a_0^{(\mathrm{I})}$ = 1.5 mm; $a_0^{(\mathrm{II})}$ = 2 mm; d=2 mm; d_c = 100 mm; $\tilde{k}_\tau=\tilde{k}_\sigma=\tilde{k}_D=\tilde{k}_{\sigma D}=\tilde{k}_{BD}=0\ \mathrm{m}^{-1}$).

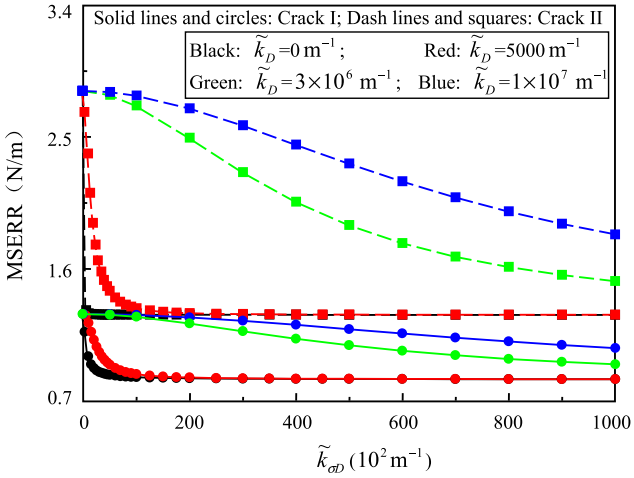

Fig. 10. Effect of electric and mechanical imperfection coupling on MSERR. ($a_0^{(\mathrm{I})}$ = 1.5 mm; $a_0^{(\mathrm{II})}$ = 2 mm; d = 2 mm; d_c = 100 mm; $\tilde{k}_\tau=\tilde{k}_\sigma=\tilde{k}_B=\tilde{k}_{\sigma B}=\tilde{k}_{BD}=0\ \mathrm{m}^{-1}$).

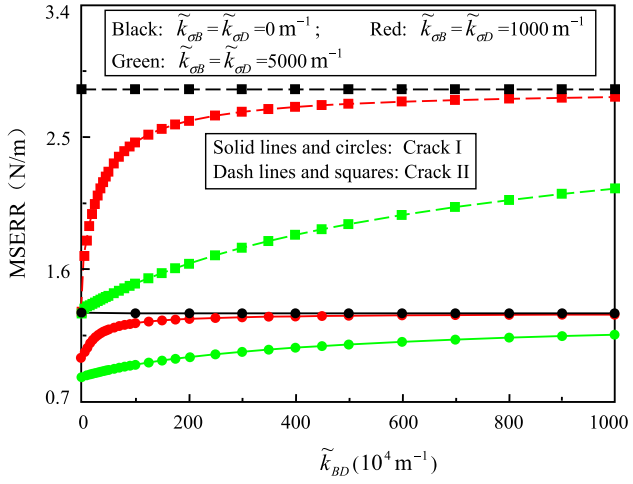

Fig. 11. Effect of magnetic and electric imperfection coupling on MSERR. ($a_0^{(\mathrm{I})}$ = 1.5 mm; $a_0^{(\mathrm{II})}$ = 2 mm; d = 2 mm; d_c = 100 mm; $\tilde{k}_\tau=\tilde{k}_\sigma=\tilde{k}_B=\tilde{k}_D=0\ \mathrm{m}^{-1}$).

the electro-mechanical imperfection coupling. When there is no coupling, the electric imperfection cannot affect MSERR; if there is coupling, the MSERR will be reduced by the electric imperfection. More serious electric imperfection plus stronger electro-mechanical imperfection coupling generally leads to more remarkable reduction of MSERR.

4.3.4. Effect of magneto-mechanical imperfection coupling

The curves of MSERR versus $\tilde{k}_{\sigma B}$ are shown in Fig. 9, with $\tilde{k}_B$ having four different values: $0\ \mathrm{m}^{-1}$, $5.0\times10^{3}\ \mathrm{m}^{-1}$, $3.0\times10^{5}\ \mathrm{m}^{-1}$ and $1.0\times10^{6}\ \mathrm{m}^{-1}$. It is seen that MSERR decreases as $\tilde{k}_{\sigma B}$ increases from $0\ \mathrm{m}^{-1}$. The more serious the magnetic imperfection is, the more steeply the MSERR curves will decrease. This again demonstrates the shielding effect of the magneto-mechanical imperfection coupling on the cracks.

In addition, if $\tilde{k}_B$ is given, only when $\tilde{k}_{\sigma B}$ varies in a finite interval can it affect MSERR. If $\tilde{k}_{\sigma B}$ is larger than the upper limit of such an interval, its effect on the cracks will become vanishingly small. Such an interval is dependent on the value of $\tilde{k}_B$. Generally, smaller $\tilde{k}_B$ (i.e., more serious magnetic imperfection) corresponds to a smaller interval.

4.3.5. Effect of electro-mechanical imperfection coupling

The effect of $\tilde{k}_{\sigma D}$ on MSERR is illustrated in Fig. 10 with $\tilde{k}_D$ varying among the four values: $0\ \mathrm{m}^{-1}$, $5.0\times10^{3}\ \mathrm{m}^{-1}$, $3.0\times10^{6}\ \mathrm{m}^{-1}$ and $1.0\times10^{7}\ \mathrm{m}^{-1}$. As expected, to increase $\tilde{k}_{\sigma D}$ from $0\ \mathrm{m}^{-1}$ will lower down MSERR, and more serious electric imperfection (i.e., smaller $\tilde{k}_D$) will lead to more steep reduction of these MSERR curves. $\tilde{k}_{\sigma D}$ can affect MSERR only when it varies in a finite interval, which depends on the magnitude of $\tilde{k}_D$. Generally, more serious electric imperfection will give rise to a smaller interval.

4.3.6. Effect of magneto-electric imperfection coupling

The curves of MSERR versus $\tilde{k}_{BD}$ are shown in Fig. 11. It is seen that whether magneto-electric imperfection coupling can affect MSERR or not is determined by the magneto-mechanical and electro-mechanical imperfection couplings. If the mechanical imperfection is decoupled from the magnetic and electric imperfections (i.e., $\tilde{k}_{\sigma B}=\tilde{k}_{\sigma D}=0\ \mathrm{m}^{-1}$), the magneto-electric imperfection coupling cannot affect MSERR. If the mechanical imperfection is coupled with the magnetic and electric imperfections (i.e., $\tilde{k}_{\sigma B}=\tilde{k}_{\sigma D}>0\ \mathrm{m}^{-1}$), as the magneto-electric imperfection coupling becomes stronger (i.e., k_{BD} becomes larger), MSERR goes up and finally converges to its value in the case of $\tilde{k}_{\sigma B}=\tilde{k}_{\sigma D}=0\ \mathrm{m}^{-1}$.

5. Conclusions

A coupling model is proposed to characterize the interfacial imperfections in a multiferroic composite. It is constructed by generalizing the traditional spring model of the imperfect interfacial region and referring to the magneto-electro-elastic constitutive relations of an perfect interfacial region between a ferromagnetic layer and another ferroelectric one. Seven parameters are introduced to describe the model with four of them representing the strength of interfacial imperfections and the other three standing for that of their couplings. It can be easily reduced to the existing non-coupled interfacial imperfection model by simply assuming the coupling parameters to have zero value, and it can be further reduced to the traditional spring model by further removing the magnetic and electric imperfections.

The intra-layer fracture problem of a composite consisting of a ferromagnetic layer, a ferroelectric layer and an intermediate imperfect interfacial region is chosen as an example to demonstrate the application of the present model. The methods of Fourier integral transform and Green's function are employed to derive the Cauchy singular integral equations for the cracks. Numerical results of the mechanical strain energy release rate (MSERR) are provided to survey the effects of the interfacial imperfections and their couplings on the fracture behavior of the composite. Three main conclusions are drawn:

- The mechanical imperfections can independently enhance MSERR. The mechanical imperfection along the thickness direction of the interfacial region has dominance over the one along the longitudinal direction.
- Only when the magnetic (or electric) imperfection is coupled with the mechanical one can the former affect MSERR. Generally, more serious magnetic (or electric) imperfection plus stronger magneto(or electro)-mechanical imperfection coupling gives rise to smaller MSERR.
- Only when the mechanical imperfection is coupled with the magnetic and electric ones can magneto-electric imperfection coupling affect MSERR. In this case, stronger magneto-electric imperfection coupling can induce larger MSERR.

Finally, it should be noted that the coupled interfacial imperfections can affect the mechanical behaviors of ferromagnetic/ferroelectric composites in many respects. The present paper only considers its application in a fracture problem. Besides, its applications in other mechanical problems such as vibration, wave propagation, buckling, and etc, still need investigation. When applying the coupled model of interfacial imperfections, one still needs to note that the thickness, h_0, of the interfacial region should be carefully specified, because it greatly affects the linear spring model. When h_0 is sufficiently large, the model is invalid; however, if h_0 is very small, nonlinear model will become more applicable.

Acknowledgements

Project supported by National Natural Science Foundation of China (Project No. 11372358).

Appendix A

$$\left.\begin{aligned}
\tilde{\mathbf{R}}^{(\mathrm{I}1)}\left(\tilde{s}_i^{(\mathrm{I})},\tilde{x}_l^{(\mathrm{I})}\right)&=a_{0i}^{(\mathrm{I})}\mathbf{R}^{(\mathrm{I}1)}\left(a_{0i}^{(\mathrm{I})}\tilde{s}_i^{(\mathrm{I})}+c_{0i}^{(\mathrm{I})},a_{0l}^{(\mathrm{I})}\tilde{x}_l^{(\mathrm{I})}+c_{0l}^{(\mathrm{I})}\right)\\
\tilde{\mathbf{R}}^{(\mathrm{II}1)}\left(\tilde{s}_j^{(\mathrm{II})},\tilde{x}_l^{(\mathrm{I})}\right)&=a_{0j}^{(\mathrm{II})}\mathbf{R}^{(\mathrm{II}1)}\left(a_{0j}^{(\mathrm{II})}\tilde{s}_j^{(\mathrm{II})}+c_{0j}^{(\mathrm{II})},a_{0l}^{(\mathrm{I})}\tilde{x}_l^{(\mathrm{I})}+c_{0l}^{(\mathrm{I})}\right)\\
\tilde{\mathbf{R}}^{(\mathrm{II}2)}\left(\tilde{s}_j^{(\mathrm{II})},\tilde{x}_m^{(\mathrm{II})}\right)&=a_{0j}^{(\mathrm{II})}\mathbf{R}^{(\mathrm{II}2)}\left(a_{0j}^{(\mathrm{II})}\tilde{s}_j^{(\mathrm{II})}+c_{0j}^{(\mathrm{II})},a_{0m}^{(\mathrm{II})}\tilde{x}_m^{(\mathrm{II})}+c_{0m}^{(\mathrm{II})}\right)\\
\tilde{\mathbf{R}}^{(\mathrm{I}2)}\left(\tilde{s}_i^{(\mathrm{I})},\tilde{x}_m^{(\mathrm{II})}\right)&=a_{0i}^{(\mathrm{I})}\mathbf{R}^{(\mathrm{I}2)}\left(a_{0i}^{(\mathrm{I})}\tilde{s}_i^{(\mathrm{I})}+c_{0i}^{(\mathrm{I})},a_{0m}^{(\mathrm{II})}\tilde{x}_m^{(\mathrm{II})}+c_{0m}^{(\mathrm{II})}\right)
\end{aligned}\right\}\tag{A-1}$$

where $\tilde{\mathbf{R}}$ and $\mathbf{R}$ are 4×4 matrices consisting of the following kernel functions

$$\left.\begin{aligned}
R_{11}^{(j1)}\left(x,s_i^{(j)}\right)&=\int_0^{+\infty}\left\{\left[F_{11}^{(j1)}(\xi)-q_{11}^{(j1)}\right]\sin(\xi x)\cos\left(\xi s_i^{(j)}\right)\right.\\
&\quad\left.-\left[G_{11}^{(j1)}(\xi)-q_{11}^{(j1)}\right]\cos(\xi x)\sin\left(\xi s_i^{(j)}\right)\right\}\mathrm{d}\xi\\
R_{1t}^{(j1)}\left(x,s_i^{(j)}\right)&=\int_0^{+\infty}\left\{\left[G_{1t}^{(j1)}(\xi)-q_{1t}^{(j1)}\right]\cos(\xi x)\cos\left(\xi s_i^{(j)}\right)\right.\\
&\quad\left.-\left[F_{1t}^{(j1)}(\xi)-q_{1t}^{(j1)}\right]\sin(\xi x)\sin\left(\xi s_i^{(j)}\right)\right\}\mathrm{d}\xi
\end{aligned}\right\}\tag{A-2}$$

$$\left.\begin{aligned} R_{21}^{(j1)}\left(x,s_i^{(j)}\right) &= \int_0^{+\infty}\left\{\left[F_{21}^{(j1)}(\xi)-q_{21}^{(j1)}\right]\cos(\xi x)\cos\left(\xi s_i^{(j)}\right)\right.\\ &\quad\left.-\left[G_{21}^{(j1)}(\xi)-q_{21}^{(j1)}\right]\sin(\xi x)\sin\left(\xi s_i^{(j)}\right)\right\}\mathrm{d}\xi\\ R_{2t}^{(j1)}\left(x,s_i^{(j)}\right) &= \int_0^{+\infty}\left\{\left[G_{2t}^{(j1)}(\xi)-q_{2t}^{(j1)}\right]\sin(\xi x)\cos\left(\xi s_i^{(j)}\right)\right.\\ &\quad\left.-\left[F_{2t}^{(j1)}(\xi)-q_{2t}^{(j1)}\right]\cos(\xi x)\sin\left(\xi s_i^{(j)}\right)\right\}\mathrm{d}\xi \end{aligned}\right\} \tag{A-3}$$

$$\left.\begin{aligned} R_{31}^{(j1)}\left(x,s_i^{(j)}\right) &= \int_0^{+\infty}\left\{\left[F_{31}^{(j1)}(\xi)-q_{31}^{(j1)}\right]\cos(\xi x)\cos\left(\xi s_i^{(j)}\right)\right.\\ &\quad\left.-\left[G_{31}^{(j1)}(\xi)-q_{31}^{(j1)}\right]\sin(\xi x)\sin\left(\xi s_i^{(j)}\right)\right\}\mathrm{d}\xi\\ R_{3t}^{(j1)}\left(x,s_i^{(j)}\right) &= \int_0^{+\infty}\left\{\left[G_{3t}^{(j1)}(\xi)-q_{3t}^{(j1)}\right]\sin(\xi x)\cos\left(\xi s_i^{(j)}\right)\right.\\ &\quad\left.-\left[F_{3t}^{(j1)}(\xi)-q_{3t}^{(j1)}\right]\cos(\xi x)\sin\left(\xi s_i^{(j)}\right)\right\}\mathrm{d}\xi \end{aligned}\right\} \tag{A-4}$$

$$\left.\begin{aligned} R_{41}^{(j1)}\left(x,s_i^{(j)}\right) &= \int_0^{+\infty}\left\{\left[F_{41}^{(j1)}(\xi)-q_{41}^{(j1)}\right]\cos(\xi x)\cos\left(\xi s_i^{(j)}\right)\right.\\ &\quad\left.-\left[G_{41}^{(j1)}(\xi)-q_{41}^{(j1)}\right]\sin(\xi x)\sin\left(\xi s_i^{(j)}\right)\right\}\mathrm{d}\xi\\ R_{4t}^{(j1)}\left(x,s_i^{(j)}\right) &= \int_0^{+\infty}\left\{\left[G_{4t}^{(j1)}(\xi)-q_{4t}^{(j1)}\right]\sin(\xi x)\cos\left(\xi s_i^{(j)}\right)\right.\\ &\quad\left.-\left[F_{4t}^{(j1)}(\xi)-q_{4t}^{(j1)}\right]\cos(\xi x)\sin\left(\xi s_i^{(j)}\right)\right\}\mathrm{d}\xi \end{aligned}\right\} \tag{A-5}$$

$$\left.\begin{aligned} R_{11}^{(j2)}\left(x,s_i^{(j)}\right) &= \int_0^{+\infty}\left\{\left[F_{11}^{(j2)}(\xi)-q_{11}^{(j2)}\right]\sin(\xi x)\cos\left(\xi s_i^{(j)}\right)\right.\\ &\quad\left.-\left[G_{11}^{(j2)}(\xi)-q_{11}^{(j2)}\right]\cos(\xi x)\sin\left(\xi s_i^{(j)}\right)\right\}\mathrm{d}\xi\\ R_{1t}^{(j2)}\left(x,s_i^{(j)}\right) &= \int_0^{+\infty}\left\{\left[G_{1t}^{(j2)}(\xi)-q_{1t}^{(j2)}\right]\cos(\xi x)\cos\left(\xi s_i^{(j)}\right)\right.\\ &\quad\left.-\left[F_{1t}^{(j2)}(\xi)-q_{1t}^{(j2)}\right]\sin(\xi x)\sin\left(\xi s_i^{(j)}\right)\right\}\mathrm{d}\xi \end{aligned}\right\} \tag{A-6}$$

$$\left.\begin{aligned} R_{21}^{(j2)}\left(x,s_i^{(j)}\right) &= \int_0^{+\infty}\left\{\left[F_{21}^{(j2)}(\xi)-q_{21}^{(j2)}\right]\cos(\xi x)\cos\left(\xi s_i^{(j)}\right)\right.\\ &\quad\left.-\left[G_{21}^{(j2)}(\xi)-q_{21}^{(j2)}\right]\sin(\xi x)\sin\left(\xi s_i^{(j)}\right)\right\}\mathrm{d}\xi\\ R_{2t}^{(j2)}\left(x,s_i^{(j)}\right) &= \int_0^{+\infty}\left\{\left[G_{2t}^{(j2)}(\xi)-q_{2t}^{(j2)}\right]\sin(\xi x)\cos\left(\xi s_i^{(j)}\right)\right.\\ &\quad\left.-\left[F_{2t}^{(j2)}(\xi)-q_{2t}^{(j2)}\right]\cos(\xi x)\sin\left(\xi s_i^{(j)}\right)\right\}\mathrm{d}\xi \end{aligned}\right\} \tag{A-7}$$

$$\left.\begin{aligned} R_{31}^{(j2)}\left(x,s_i^{(j)}\right) &= \int_0^{+\infty}\left\{\left[F_{31}^{(j2)}(\xi)-q_{31}^{(j2)}\right]\cos(\xi x)\cos\left(\xi s_i^{(j)}\right)\right.\\ &\quad\left.-\left[G_{31}^{(j2)}(\xi)-q_{31}^{(j2)}\right]\sin(\xi x)\sin(\xi s_i^{(j)})\right\}\mathrm{d}\xi\\ R_{3t}^{(j2)}\left(x,s_i^{(j)}\right) &= \int_0^{+\infty}\left\{\left[G_{3t}^{(j2)}(\xi)-q_{3t}^{(j2)}\right]\sin(\xi x)\cos(\xi s_i^{(j)})\right.\\ &\quad\left.-\left[F_{3t}^{(j2)}(\xi)-q_{3t}^{(j2)}\right]\cos(\xi x)\sin\left(\xi s_i^{(j)}\right)\right\}\mathrm{d}\xi \end{aligned}\right\} \tag{A-8}$$

$$\left.\begin{aligned} R_{41}^{(j2)}\left(x,s_i^{(j)}\right) &= \int_0^{+\infty}\left\{\left[F_{41}^{(j2)}(\xi)-q_{41}^{(j2)}\right]\cos(\xi x)\cos\left(\xi s_i^{(j)}\right)\right.\\ &\quad\left.-\left[G_{41}^{(j2)}(\xi)-q_{41}^{(j2)}\right]\sin(\xi x)\sin\left(\xi s_i^{(j)}\right)\right\}\mathrm{d}\xi\\ R_{4t}^{(j2)}\left(x,s_i^{(j)}\right) &= \int_0^{+\infty}\left\{\left[G_{4t}^{(j2)}(\xi)-q_{4t}^{(j2)}\right]\sin(\xi x)\cos\left(\xi s_i^{(j)}\right)\right.\\ &\quad\left.-\left[F_{4t}^{(j2)}(\xi)-q_{4t}^{(j2)}\right]\cos(\xi x)\sin\left(\xi s_i^{(j)}\right)\right\}\mathrm{d}\xi \end{aligned}\right\} \tag{A-9}$$

$$F_{1t}^{(j1)}(\xi)=\sum_{n=1}^{6}\alpha_{nt}^{(j)}Q_{sn}^{(1)}(\xi,h_{\mathrm{I}});\quad G_{1t}^{(j1)}(\xi)=\sum_{n=1}^{6}\beta_{nt}^{(j)}Q_{an}^{(1)}(\xi,h_{\mathrm{I}}) \tag{A-10}$$

$$F_{2t}^{(j1)}(\xi)=\sum_{n=1}^{6}\alpha_{nt}^{(j)}P_{sn}^{(1)}(\xi,h_{\mathrm{I}});\quad G_{2t}^{(j1)}(\xi)=\sum_{n=1}^{6}\beta_{nt}^{(j)}P_{an}^{(1)}(\xi,h_{\mathrm{I}}) \tag{A-11}$$

$$F_{3t}^{(j1)}(\xi)=\sum_{n=1}^{6}\alpha_{nt}^{(j)}S_{sn}^{(1)}(\xi,h_{\mathrm{I}});\quad G_{3t}^{(j1)}(\xi)=\sum_{n=1}^{6}\beta_{nt}^{(j)}S_{an}^{(1)}(\xi,h_{\mathrm{I}}) \tag{A-12}$$

$$F_{4t}^{(j1)}(\xi)=\sqrt{\epsilon_{11}^{(1)}\epsilon_{33}^{(1)}}\left[\mathrm{e}^{-\bar{\epsilon}\xi h_{\mathrm{I}}}\alpha_{8t}^{(j)}-\mathrm{e}^{\bar{\epsilon}\xi h_{\mathrm{I}}}\alpha_{7t}^{(j)}\right];$$
$$G_{4t}^{(j1)}(\xi)=\sqrt{\epsilon_{11}^{(1)}\epsilon_{33}^{(1)}}\left[\mathrm{e}^{-\bar{\epsilon}\xi h_{\mathrm{I}}}\beta_{8t}^{(j)}-\mathrm{e}^{\bar{\epsilon}\xi h_{\mathrm{I}}}\beta_{7t}^{(j)}\right] \tag{A-13}$$

$$F_{1t}^{(j2)}(\xi)=\sum_{n=1}^{6}\alpha_{(n+16)t}^{(j)}Q_{sn}^{(2)}(\xi,-h_{\mathrm{II}});$$
$$G_{1t}^{(j1)}(\xi)=\sum_{n=1}^{6}\beta_{(n+16)t}^{(j)}Q_{an}^{(2)}(\xi,-h_{\mathrm{II}}) \tag{A-14}$$

$$F_{2t}^{(j2)}(\xi)=\sum_{n=1}^{6}\alpha_{(n+16)t}^{(j)}P_{sn}^{(2)}(\xi,-h_{\mathrm{II}});$$
$$G_{2t}^{(j2)}(\xi)=\sum_{n=1}^{6}\beta_{(n+16)t}^{(j)}P_{an}^{(2)}(\xi,-h_{\mathrm{II}}) \tag{A-15}$$

$$F_{3t}^{(j2)}(\xi)=\sqrt{\mu_{11}^{(2)}\mu_{33}^{(2)}}\left[\alpha_{(24)t}^{(j)}\mathrm{e}^{\tilde{\mu}\xi h_{\mathrm{II}}}-\alpha_{(23)t}^{(j)}\mathrm{e}^{-\tilde{\mu}\xi h_{\mathrm{II}}}\right];$$
$$G_{3t}^{(j2)}(\xi)=\sqrt{\mu_{11}^{(2)}\mu_{33}^{(2)}}\left[\beta_{(24)t}^{(j)}\mathrm{e}^{\tilde{\mu}\xi h_{\mathrm{II}}}-\beta_{(23)t}^{(j)}\mathrm{e}^{-\tilde{\mu}\xi h_{\mathrm{II}}}\right] \tag{A-16}$$

$$F_{4t}^{(j2)}(\xi)=\sum_{n=1}^{6}\alpha_{(n+16)t}^{(j)}S_{sn}^{(2)}(\xi,-h_{\mathrm{II}});$$
$$G_{4t}^{(j2)}(\xi)=\sum_{n=1}^{6}\beta_{(n+16)t}^{(j)}S_{an}^{(2)}(\xi,-h_{\mathrm{II}}) \tag{A-17}$$

where $j=\mathrm{I},\ \mathrm{II}$ and $t=2,3,4$. The subscript 's' and 'a' denote the symmetric and anti-symmetric sub-problems induced by the even and odd parts of the GPD, respectively. $\bar{\epsilon}=\sqrt{\epsilon_{11}^{(1)}/\epsilon_{33}^{(1)}}$ and $\tilde{\mu}=\sqrt{\mu_{11}^{(2)}/\mu_{33}^{(2)}}$. Q_n, P_n and S_n are known functions inferred from the constitutive relations in Eq. (8) (Li et al., 2011). $\alpha_{np}^{(j)}$ and $\beta_{np}^{(j)}$ ($j=\mathrm{I},\ \mathrm{II}; n=1,2,\ldots,24;\ p=1,2,3,4$) are elements of $\mathbf{M}_{js}^{-1}$ and $\mathbf{M}_{ja}^{-1}$. $\mathbf{M}_{js}$ and $\mathbf{M}_{ja}$ are the coefficient matrices of the algebraic equations transformed from the boundary conditions of the symmetric and anti-symmetric sub-problems, respectively.

$$\mathbf{q}_j=\{q_{rp}^{(ji)}\}_{4\times4}(r=1,2,3,4;\ p=1,2,3,4;\ j=\mathrm{I},\ \mathrm{II};\ i=1,2) \tag{A-18}$$

$$q_{rp}^{(ji)}=\lim_{\xi\to\infty}F_{rp}^{(ji)}(\xi)=\lim_{\xi\to\infty}G_{rp}^{(ji)}(\xi)(r=1,2,3,4;\ p=1,2,3,4;$$
$$j=\mathrm{I},\ \mathrm{II};\ i=1,2) \tag{A-19}$$

where the limits including $q_{rp}^{(\mathrm{I2})}$, $q_{rp}^{(\mathrm{II1})}$, $q_{t1}^{(\mathrm{I1})}$, $q_{1t}^{(\mathrm{I1})}$, $q_{t1}^{(\mathrm{II2})}$ and $q_{1t}^{(\mathrm{II2})}$ ($r=1,2,3,4; p=1,2,3,4;\ t=2,3,4$) simultaneously have zero values, while all the other limits are nonzero.

References

Benveniste, Y., 2009. An interface model for a three-dimensional curved thin piezoelectric interphase between two piezoelectric media. Math. Mech. Solids 14 (1–2), 102–122.

Benveniste, Y., Miloh, T., 2001. Imperfect soft and stiff interfaces in two-dimensional elasticity. Mech. Mater. 33 (6), 309–323.

Bichurin, M.I., Viehland, D., Srinivasan, G., 2007. Magnetoelectric interactions in ferromagnetic-piezoelectric layered structures: phenomena and devices. J. Electroceram. 19 (4), 243–250.

Chan, Y.S., Paulino, G.H., Fannjiang, A.C., 2001a. The crack problem for nonhomogeneous materials under antiplane shear loading – a displacement based formulation. Int. J. Solids Struct. 38 (17), 2989–3005.

Chan, Y.S., Fannjiang, A.C., Paulino, G.H., 2001b. Integral equations with hypersingular kernels – theory and applications to fracture mechanics. Int. J. Eng. Sci. 41 (7), 683–720.

Chen, W.Q., Lee, K.Y., 2004. Exact solution of angle-ply piezoelectric laminates in cylindrical bending with interfacial imperfections. Compos. Struct. 65 (3–4), 329–337.

Chen, W.Q., Wang, Y.F., Cai, J.B., Ye, G.R., 2004. Three-dimensional analysis of cross-ply laminated cylindrical panels with weak interfaces. Int. J. Solids Struct. 41 (9–10), 2429–2446.

Choi, H.J., 1997. A periodic array of cracks in a functionally graded nonhomogeneous medium loaded under in-plane normal and shear. Int. J. Fract. 88 (2), 107–128.
Eerenstein, W., Mathur, N.D., Scott, J.F., 2006. Multiferroic and magnetoelectric materials. Nature 442 (7104), 759–765.
Erdogan, F., 1985. The crack problem for bonded nonhomogeneous materials under antiplane shear loading. J. Appl. Mech. 52 (4), 823–828.
Erdogan, F., Gupta, G.D., 1972. On the numerical solution of singular integral equations. Q. Appl. Math. 29 (4), 525–534.
Fan, H., Wang, G.F., 2003. Screw dislocation interacting with imperfect interface. Mech. Mater. 35 (10), 943–953.
Fang, Q.H., Liu, Y.W., Jin, B., Wen, P.H., 2009. A piezoelectric screw dislocation in a three-phase composite cylinder model with an imperfect interface. Int. J. Eng. Sci. 47 (1), 39–49.
Gu, S.T., He, Q.C., 2011. Interfacial discontinuity relations for coupled multifield phenomena and their application to the modeling of thin interphases as imperfect interfaces. J. Mech. Phys. Solids 59 (7), 1413–1426.
Gu, S.T., Qin, L., Zhu, Q.Z., 2014. Variational principles and size-dependent bounds for piezoelectric inhomogeneous materials with piezoelectric spring–layer imperfect interfaces. Smart Mater. Struct. 23 (5), 055003.
Guessasma, S., Benseddiq, N., Lourdin, D., 2010. Effective Young's modulus of biopolymer composites with imperfect interface. Int. J. Solids Struct. 47 (18–19), 2436–2444.
Hashin, Z., 1990. Thermoelastic properties of fiber composites with imperfect interface. Mech. Mater. 8 (4), 333–348.
Hashin, Z., 1991. The spherical inclusion with imperfect interface. J. Appl. Mech. 58 (2), 444–449.
Hashin, Z., 2002. Thin interphase/imperfect interface in elasticity with application to coated fiber composites. J. Mech. Phys. Solids 50 (12), 2509–2537.
Huang, J., Kuo, W.S., 1997. The analysis of piezoelectric/piezomagnetic composite materials containing ellipsoidal inclusions. J. Appl. Phys. 81 (3), 1378–1386.
Huang, Y., Li, X.F., Lee, K.Y., 2009. Interfacial shear horizontal (SH) waves propagating in a two-phase piezoelectric/piezomagnetic structure with an imperfect interface. Philos. Mag. Lett. 89 (1), 95–103.
Kuo, H.Y., 2013. Effective property of multiferroic fibrous composites with imperfect interfaces. Smart. Mater. Struct. 22 (10), 105005.
Kushch, V.I., Chernobai, V.S., 2014. Transverse conductivity and longitudinal shear of elliptic fiber composite with imperfect interface. Int. J. Solids Struct. 51 (13), 2529–2538.
Li, P., Jin, F., 2014. Effect of an imperfect interface in a quartz crystal microbalance for detecting the properties of an additional porous layer. J. Appl. Phys. 115 (5), 054502.
Li, Y.D., Lee, K.Y., 2009. Crack tip shielding and anti-shielding effects of the imperfect interface in a layered piezoelectric sensor. Int. J. Solids Struct. 46 (7–8), 1736–1742.
Li, Y.D., Lee, K.Y., 2010. Two collinear unequal cracks in a poled piezoelectric plane: mode I case solved by a new approach of real fundamental solutions. Int. J. Fract. 165 (1), 47–60.
Li, Y.D., Lee, K.Y., Feng, F.X., Pan, J.W., 2011. Mode I fracture analysis of a piezoelectric strip based on real fundamental solutions. Eur. J. Mech. A/Solids 30 (2), 158–166.
Li, Y.D., Zhao, H., Zhang, Nan, 2013. Mixed mode fracture of a piezoelectric–piezomagnetic bi-layer structure with two un-coaxial cracks parallel to the interface and each in a layer. Int. J. Solids Struct. 50 (22–23), 3610–3617.
Liu, C.B., Bian, Z.G., Chen, W.Q., Lü, C.F., 2014. Three-dimensional pyroelectric analysis of a multilayered piezoelectric hollow sphere with imperfect bonding. Compos. Struct. 113 (1), 145–154.
Mishuris, G., Movchan, N.V., Movchan, A.B., 2006. Steady-state motion of a mode-III crack on imperfect interfaces. Q. J. Mech. Appl. Math. 59 (4), 487–516.
Mishuris, G., Piccolroaz, A., Vellender, A., 2014. Boundary integral formulation for cracks at imperfect interfaces. Q. J. Mech. Appl. Math. 67 (3), 363–387.
Morini, L., Piccolroaz, A., Mishuris, G., Radi, E., 2013. Integral identities for a semi-infinite interfacial crack in anisotropic elastic bimaterials. Int. J. Solids Struct. 50 (9), 1437–1448.
Muskhelishvili, N.I., 1953a. Singular Integral Equations. Noordhoff, Groningen, The Netherlands.
Muskhelishvili, N.I., 1953b. Some Basic Problems of The Mathematical Theory of Elasticity. Noordhoff, Groningen, The Netherlands.
Nairn, J.A., 2007. Numerical implementation of imperfect interfaces. Comput. Mater. Sci. 40 (4), 525–536.
Needleman, A., 1987. A continuum model for void nucleation by inclusion debonding. J. Appl. Mech. 54 (3), 525–531.
Needleman, A., 1990. An analysis of decohesion along an imperfect interface. Int. J. Fract. 42 (1), 21–40.
Otero, J.A., Rodríguez-Ramos, R., Bravo-Castillero, J., Monsivais, G., 2012. Interfacial waves between two piezoelectric half-spaces with electro-mechanical imperfect interface. Philos. Mag. Lett. 92 (10), 534–540.
Otero, J.A., Rodríguez-Ramos, R., Monsivais, G., Stern, C., Lebon, F., 2013. Interfacial waves between piezoelectric and piezomagnetic half-spaces with magneto-electro-mechanical imperfect interface. Philos. Mag. Lett. 93 (7), 413–421.
Park, S., Sun, C.T., 1995. Fracture criterion for piezoelectric ceramics. J. Am. Ceram. Soc. 78 (6), 1475–1480.
Piccolroaz, A., Mishuris, G., 2013. Integral identities for a semi-infinite interfacial crack in 2D and 3D elasticity. J. Elast. 110 (2), 117–140.
Rizzoni, R., Lebon, F., 2013. Imperfect interfaces as asymptotic models of thin curved elastic adhesive interphases. Mech. Res. Comm. 51 (1), 39–50.
Shi, Y., Wan, Y., Zhong, Z., 2014. Variational bounds for the effective electroelastic moduli of piezoelectric composites with electromechanical coupling spring-type interfaces. Mech. Mater. 72 (1), 72–93.
Spaldin, N.A., Fiebig, M., 2005. The renaissance of magnetoelectric multiferroics. Science 309 (5733), 391–392.
Sudak, L.J., Ru, C.Q., Schiavone, P., Mioduchowski, A., 1999. A circular inclusion with inhomogeneously imperfect interface in plane elasticity. J. Elast. 55 (1), 19–41.
Sun, W.H., Ju, G.L., Pan, J.W., Li, Y.D., 2011. Effects of the imperfect interface and piezoelectric/piezomagnetic stiffening on the SH wave in a multiferroic composite. Ultrasonics 51 (7), 831–838.
Theocaris, P.S., Ioakimids, N.I., 1977. Numerical integration methods for the solution of singular integral equations. Q. Appl. Math. 35 (2), 173–183.
Vellender, A., Mishuris, G., Piccolroaz, A., 2013. Perturbation analysis for an imperfect interface crack problem using weight function techniques. Int. J. Solids Struct. 50 (24), 4098–4107.
Wang, H.M., 2011. Dynamic electromechanical behavior of a triple-layer piezoelectric composite cylinder with imperfect interfaces. Appl. Math. Modell. 35 (4), 1765–1781.
Wang, X., Pan, E., 2007. Magnetoelectric effects in multiferroic fibrous composite with imperfect interface. Phys. Rev. B 76 (21), 214107.
Wang, X., Sudak, L.J., Pan, E., 2008. Uniform stresses inside an elliptical inhomogeneity with an imperfect interface in plane elasticity. J. Appl. Mech. 75 (5), 054501.
Wang, Z., Zhu, J., Jin, X.Y., Chen, W.Q., Zhang, C., 2014. Effective moduli of ellipsoidal particle reinforced piezoelectric composites with imperfect interfaces. J. Mech. Phys. Solids 65 (1), 138–156.
Xue, Y., Liu, J.X., 2010. Decay rate of saint-venant end effects for plane deformations of piezoelectric-piezomagnetic sandwich structures. Acta Mech. Sol. Sin. 23 (5), 407–419.
Yuan, L., Du, J.K., Ma, T., Wang, J., 2014. Study on SH-SAW in imperfectly bonded piezoelectric structures loaded with viscous liquid. Acta Mech. 225 (1), 1–11.
Zhao, M.H., Fan, C.Y., 2008. Strip electric–magnetic breakdown model in magnetoelectroelastic medium. J. Mech. Phys. Solids 56 (12), 3441–3458.
Zheng, H., Wang, J., Lofland, S.E., et al., 2004. Multiferroic $BaTiO_3$–$CoFe_2O_4$ Nanostructures. Science 303 (5658), 661–663.
Zhong, X.C., Lee, K.Y., 2011. A dielectric crack in a functionally graded piezoelectric layer. Eur. J. Mech. A/Solids 30 (6), 761–769.
Zhong, X.C., Li, X.F., Lee, K.Y., 2009a. Analysis of a mode-I crack perpendicular to an imperfect interface. Int. J. Solids Struct. 46 (6), 1456–1463.
Zhong, X.C., Liu, F., Li, X.F., 2009b. Transient response of a magnetoelectroelastic solid with two collinear dielectric cracks under impacts. Int. J. Solids Struct. 46 (14–15), 2950–2958.
Zhou, Y.T., Li, X., Yu, D.H., 2010. A partially insulated interface crack between a graded orthotropic coating and a homogeneous orthotropic substrate under heat flux supply. Int. J. Solids Struct. 47 (6), 768–778.
Zhu, B.J., Qin, T.Y., 2007. Hypersingular integral equation method for a three-dimensional crack in anisotropic electro-magneto-elastic bimaterials. Theor. Appl. Fract. Mech. 47 (3), 219–232.